The Astrophysical Journal, 895:37 (13pp), 2020 May 20 https://doi.org/10.3847/1538-4357/ab8cc4

Resolving the Soft X-Ray Ultrafast Outflow in PDS 456

J. N. Reeves[1,2], V. Braito[1,2], G. Chartas[3], F. Hamann[4], S. Laha[1,5], and E. Nardini[6,7]
[1] Center for Space Science and Technology, University of Maryland Baltimore County, 1000 Hilltop Circle, Baltimore, MD 21250, USA; jreeves@umbc.edu
[2] INAF, Osservatorio Astronomico di Brera, Via Bianchi 46 I-23807 Merate (LC), Italy
[3] Department of Physics and Astronomy, College of Charleston, Charleston, SC 29424, USA
[4] Department of Physics & Astronomy, University of California, Riverside, CA 92507, USA
[5] Astrophysics Particle Laboratory, NASA/Goddard Space Flight Center, Mail Code 661, Greenbelt, MD 20771, USA
[6] INAF, Osservatorio Astrofisico di Arcetri, Largo Enrico Fermi 5, I-50125 Firenze, Italy
[7] Dipartimento di Fisica e Astronomia, Università di Firenze, via G. Sansone 1, I-50019 Sesto Fiorentino, Firenze, Italy
Received 2020 March 2; revised 2020 April 20; accepted 2020 April 22; published 2020 May 22

Abstract

Past X-ray observations of the nearby luminous quasar PDS 456 (at $z = 0.184$) have revealed a wide-angle accretion disk wind with an outflow velocity of $\sim -0.25c$, as observed through observations of its blueshifted iron K-shell absorption line profile. Here we present three new XMM-Newton observations of PDS 456: one in 2018 September where the quasar was bright and featureless and two in 2019 September, 22 days apart, occurring when the quasar was five times fainter and where strong blueshifted lines from the wind were present. During the second 2019 September observation, three broad ($\sigma = 3000\,\mathrm{km\,s^{-1}}$) absorption lines were resolved in the high-resolution Reflection Grating Spectrometer spectrum that are identified with blueshifted O VIII Lyα, Ne IX Heα, and Ne X Lyα. The outflow velocity of this soft X-ray absorber was found to be $v/c = -0.258 \pm 0.003$, fully consistent with an iron K absorber with $v/c = -0.261 \pm 0.007$. The ionization parameter and column density of the soft X-ray component ($\log \xi = 3.4$, $N_{\rm H} = 2 \times 10^{21}\,\mathrm{cm^{-2}}$) outflow was lower by about 2 orders of magnitude when compared to the high-ionization wind at iron K ($\log \xi = 5$, $N_{\rm H} = 7 \times 10^{23}\,\mathrm{cm^{-2}}$). Substantial variability was seen in the soft X-ray absorber between the 2019 observations, declining from $N_{\rm H} = 10^{23}$ to $10^{21}\,\mathrm{cm^{-2}}$ over 20 days, while the iron K component was remarkably stable. We conclude that the soft X-ray wind may originate from an inhomogeneous wind streamline passing across the line of sight that, due to its lower ionization, is located further from the black hole, on parsec scales, than the innermost disk wind.

Unified Astronomy Thesaurus concepts: Active galactic nuclei (16); Radio quiet quasars (1354); X-ray active galactic nuclei (2035); Black hole physics (159); X-ray quasars (1821)

1. Introduction

The discovery of blueshifted absorption features from K-shell transitions of iron has provided strong evidence for the presence of high-velocity outflows in active galactic nuclei (AGN). The measured blueshifts imply outflow velocities of the order of $\sim -0.1c$ or higher (e.g., APM 08279+5255, Chartas et al. 2002; PG 1211+143, Pounds et al. 2003; PDS 456, Reeves et al. 2003). The high velocities and ionization of the material (from He and H-like Fe) suggest that the high-velocity outflows originate from much closer to the black hole than the slower, less ionized warm absorbers (e.g., Kaastra et al. 2000; Kaspi 2002; Crenshaw et al. 2003; McKernan et al. 2007). Systematic studies of archival XMM-Newton (Tombesi et al. 2010, 2011) and Suzaku (Gofford et al. 2013) data, as well as X-ray variability studies (Igo et al. 2020), have shown that high-velocity iron K winds may be a common feature of nearby AGN. The derived outflow rates are calculated to be high (up to $\sim$few $M_{\odot}\,\mathrm{yr^{-1}}$) and therefore comparable with the measured accretion rates of AGN, while the outflows are estimated to carry kinetic power as much as a few percent of the bolometric luminosity, $L_{\rm bol}$ (Tombesi et al. 2012; Gofford et al. 2015). As such, they may play an important role in linking black hole growth and the properties of the host galaxy (King 2003, 2010) and offer a possible interpretation of the $M - \sigma$ relation for galaxies (Ferrarese & Merritt 2000; Gebhardt 2000).

While the evidence for ultrafast outflows in the Fe K band is now well established, there has been a relative scarcity of detections to date in the soft X-ray band. Detecting lower-ionization, soft-band counterparts of high-velocity outflows is important in order to probe all phases of the outflowing gas and its structure across a wide range of ionization and column density. Indeed, the original evidence for the fast wind seen in PG 1211+143 (Pounds et al. 2003) came from both its iron K profile and blueshifted soft X-ray lines in the XMM-Newton Reflection Grating Spectrometer (RGS) spectrum and was subsequently confirmed in analysis of later data sets (Pounds et al. 2016; Reeves et al. 2018).

During an initial XMM-Newton observation of the nearby QSO PDS 456 in 2001, Reeves et al. (2003) first noted the presence of blueshifted absorption in the soft X-ray band. A broad absorption trough was resolved in the RGS spectrum, attributed to a blend of L-shell transitions from highly ionized Fe near $\sim$1 keV, with an estimated outflow velocity of $\sim -50{,}000\,\mathrm{km\,s^{-1}}$, in addition to the now well-established high-velocity outflow detected in the Fe K band (Reeves et al. 2009; Nardini et al. 2015; Matzeu et al. 2017a), where the outflow velocity has been confirmed to vary over a narrow range between $0.25c$ and $0.30c$. The presence of high-velocity, soft-band counterparts of the outflow in PDS 456 has since been confirmed in a multi-epoch analysis of all of the archival XMM-Newton observations of PDS 456 (Reeves et al. 2016), although the soft X-ray velocities did not always match those measured in the iron K-shell band.

Concerning other AGN, a soft-band absorber with a velocity of $\sim -0.25c$ was also observed in IRAS 13224−3809 through high-resolution RGS data (Pinto et al. 2018), where the

corresponding highly ionized Fe K counterpart has a similar velocity to the soft X-ray lines (Parker et al. 2017). The narrow-line Seyfert 1 galaxy 1H 0707−495, which has a very similar nature to IRAS 13224−3809, also appears to show a variety of blueshifted absorption line features associated with a fast wind with XMM-Newton at a velocity of $\sim 0.13c$ (Kosec et al. 2018). Curiously, this AGN also displays soft X-ray emission lines that are blueshifted by up to 8000 km s^{-1}, which Kosec et al. (2018) interpreted in the framework of a slowing, cooling outflow on larger scales. A fast soft X-ray outflow was observed in the XMM-Newton RGS spectrum of the narrow-line Seyfert 1 galaxy IRAS 17020+4544 (Longinotti et al. 2015), covering a wide range of ionization and column density with outflow velocities in the range −23,000 to −33,000 km s^{-1}, although an iron K-shell counterpart to this wind has not yet been reported. Further claims of soft X-ray fast wind detections noted in the literature include Ark 564 (Gupta et al. 2013) and Mrk 590 (Gupta et al. 2015), in these cases performed with the gratings on board Chandra, although with no known iron K-shell component. Thus, while the evidence for soft X-ray components of ultrafast outflows is growing, the exact relationship between the iron K and soft X-ray fast winds is still poorly understood

Here we present three new observations of PDS 456 from 2018 to 2019 taken with XMM-Newton, of which two were also simultaneous with NuSTAR, that are described further below. As discussed above, the radio-quiet quasar PDS 456 (at $z = 0.184$; Torres et al. 1997) was one of the first prototype examples of an ultrafast outflow. Indeed, since its initial detection in 2001 with XMM-Newton (Reeves et al. 2003), the presence of the ultrafast outflow in PDS 456 has now been established through over a decade's worth of X-ray observations (Reeves et al. 2009, 2014, 2018a, 2018b; Behar et al. 2010; Gofford et al. 2014; Hagino et al. 2015; Nardini et al. 2015; Matzeu et al. 2016, 2017a, 2017b; Parker et al. 2018; Boissay-Malaquin et al. 2019). Furthermore, Hamann et al. (2018) recently claimed a fast UV counterpart to the X-ray wind on the basis of a broad C IV trough predicted from photoionization modeling.

In this paper, we reveal the structure of the wind through the detection of resolved soft X-ray absorption lines in the XMM-Newton RGS, which, as we will show, exactly match the outflow velocity of the wind as measured in the iron K band. Furthermore, from the wind variability, we also probe the location and properties of the soft X-ray wind component.

2. Observations and Data Reduction

Over 2018–2019, PDS 456 was observed a further three times with XMM-Newton as part of a new campaign to study the long-term variability of its X-ray ultrafast outflow and its possible connection to the UV wind. A summary of the overall campaign is listed in Table 1. Note that the observation in 2018 September was performed simultaneously with NuSTAR and the Hubble Space Telescope (HST), the second observation in early 2019 September (hereafter 2019a) was coordinated with HST, and the third observation in late 2019 September (hereafter 2019b) was simultaneous with NuSTAR. All XMM-Newton observations were performed in Large Window mode in the pn and MOS to mitigate any photon pileup.

The X-ray observations were processed using the NUSTARDAS v1.8.0, XMM-Newton SAS v18.0, and HEASOFT v6.25 software. NuSTAR source spectra were extracted using a 50″ circular region centered on the source and background from a 76″ circular region clear from stray light. The XMM-Newton EPIC-pn spectra were extracted from single and double events using a 30″ source region and 2″ × 34″ background regions on the same chip. The spectra and responses from the individual MOS 1 and MOS 2 CCDs were combined into a single spectrum after they were first checked for consistency, as were the individual spectra from the FPMA and FPMB detectors on board NuSTAR. The NuSTAR and XMM-Newton pn and MOS spectra are binned to at least 50 counts bin^{-1}. Spectra from the XMM-Newton RGS (den Herder et al. 2001) were extracted using the RGSPROC pipeline and combined into a single spectrum for each of the observations, after first checking that the individual RGS 1 and RGS 2 spectra were consistent with each other within the errors.

Table 1
Log of 2018–2019 PDS 456 XMM-Newton Observations

	2018	2019a	2019b
ObsID	0830390101	0830390201	0830390401
Start date	2018 Sep 20	2019 Sep 2	2019 Sep 24
Start time (UT)	13:18:00	15:24:15	13:53:32
Duration[a]	86.0	83.0	94.3
Net rate[b]	3.958 ± 0.008	0.821 ± 0.004	1.254 ± 0.004
Flux[c]	9.43	1.87	2.24
Coverage[d]	HST + NuSTAR	HST	NuSTAR

Notes.
[a] Total duration of exposure in kiloseconds with XMM-Newton EPIC-pn.
[b] Net count rates (counts s^{-1}) over the 0.4–10 keV band for XMM-Newton EPIC-pn.
[c] Flux in the 2–10 keV band compared to an absorbed power law in units $\times 10^{-12}$ erg cm^{-2} s^{-1}.
[d] Coordinated with either HST/COS or NuSTAR (or both). All observations have Swift coverage.

2.1. Overview of the New Campaign

In order to provide an overview of the whole campaign, Figure 1 (left panel) shows the broadband XMM-Newton EPIC-pn and NuSTAR X-ray spectra obtained for the three observations. The observations captured significant variability of the QSO. The 2018 observation caught PDS 456 in a very bright state (where $F_{2-10} = 9.4 \times 10^{-12}$ erg cm^{-2} s^{-1}) following a major X-ray flare that occurred during the Swift monitoring. The X-ray spectrum of this epoch is continuum-dominated, while the soft X-ray spectrum (as seen by the RGS) is featureless. Details of the 2018 observation, the possible presence of a high-energy cutoff in the NuSTAR spectrum, the X-ray flare as seen by concurrent Swift monitoring, and the inferred X-ray coronal properties of PDS 456 will be discussed in a subsequent paper.

In comparison, the two 2019 observations are a factor of 5 fainter over the 2–10 keV band compared to the bright 2018 observation. Both 2019 observations show similar pronounced iron K absorption over the 7–10 keV band. Of these, the 2019a spectrum is more obscured at soft X-rays and about 50% fainter than the 2019b spectrum below 2 keV. Indeed, Figure 1 (right panel) shows the Swift X-ray Telescope (XRT) light curve over the 0.3–10 keV band obtained during the 2019 campaign, where the 2019a XMM-Newton observation occurred near a period of minimum flux. The 2019b XMM-Newton observation is at a typical flux level for the 2019 monitoring

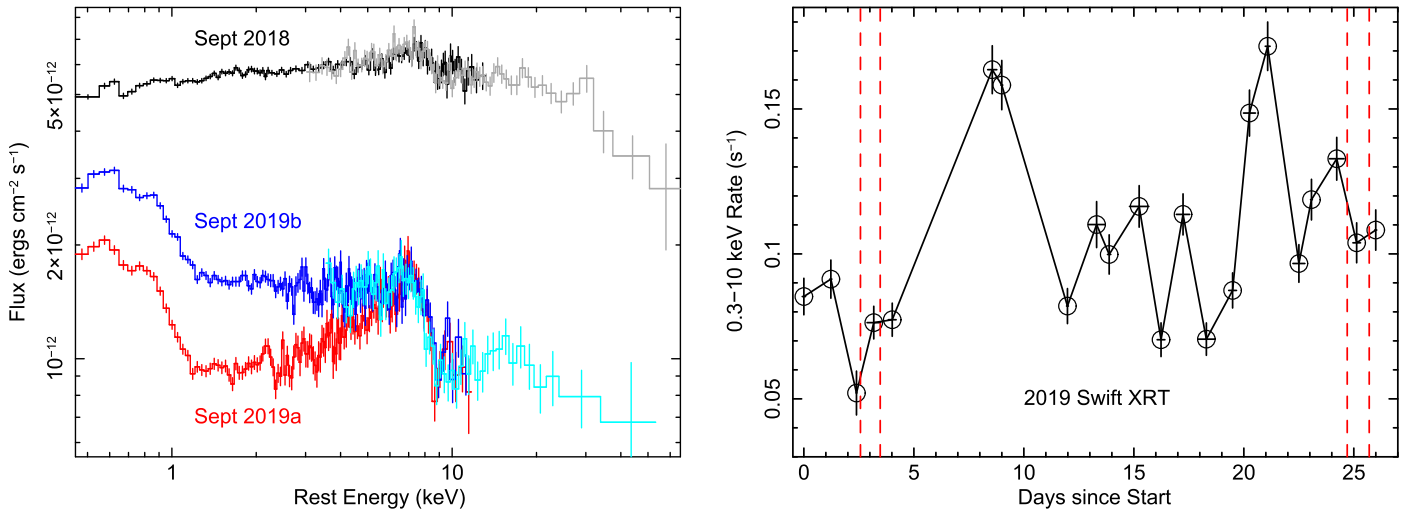

Figure 1. Left panel: broadband XMM-Newton and NuSTAR X-ray spectra of the three observations of PDS 456, observed from 2018 September to 2019 September (see Table 1 for details). The 2018 September spectrum is plotted in black (gray scale for NuSTAR), the first of the 2019 September spectra in red (2019a), and the second September observation (2019b) in blue (cyan for NuSTAR). Note that the spectra are plotted against a simple $\Gamma = 2$ power law to create νF_ν spectra and corrected for the Galactic absorption column. The campaign captured strong variability from PDS 456. The 2018 observation was observed in a high flux state, which followed a major flare as seen during monitoring with Swift. Its X-ray spectrum is mainly featureless, except for a rollover present above 10 keV seen in NuSTAR due to a high-energy cutoff. In contrast, the 2019 spectra are at least a factor of 5 lower in flux and show pronounced absorption at iron K in the 7–10 keV band, while the 2019a spectrum also shows strong soft X-ray absorption. Right panel: 2019 Swift XRT light curve, performed from 2019 August 31 to 2019 September 26. The vertical dashed lines show the intervals of the two 2019 XMM-Newton pointings, where the 2019a observation occurred near a minimum in the light curve.

campaign, although this is still at a much lower flux than in 2018.

In this paper, we concentrate our initial analysis on the 2019b observation, while we also compare the results to the spectra obtained in the 2018 and 2019a epochs to test the wind variability. As we will subsequently show, the 2019b observation captured PDS 456 in a wind-dominated state, where we resolve multiple absorption line profiles from the outflow both in the soft X-ray band with XMM-Newton RGS and at iron K in the broadband spectrum. In contrast, the 2019a observation caught the source in a more obscured state, where its very low soft X-ray flux prohibits a detailed analysis of the RGS spectrum. The simultaneous HST/Cosmic Origins Spectrograph (COS) spectroscopy of PDS 456 (PI: F. Hamann), coincident with the 2018 and 2019a observations, where the motivation was to further monitor the outflowing UV absorption toward PDS 456, will be presented in later work. Note that outflow velocities are given with respect to the rest frame of the host galaxy of PDS 456 at $z = 0.184$ after correcting for relativistic Doppler shifts. Errors are quoted at 90% confidence for one interesting parameter (or $\Delta\chi^2 = 2.7$).

3. Soft X-Ray Spectral Analysis

3.1. The XMM-Newton RGS Spectrum

We first analyze the soft X-ray spectrum of PDS 456 from the 2019b observation, obtained with the XMM-Newton RGS. The total exposure of the RGS observation is 92.4 ks, while the net count rate for the combined RGS 1+2 spectrum is 0.070 ± 0.001 counts s^{-1}, yielding ~6500 net counts. The RGS spectrum was grouped into bins of width $\Delta\lambda = 0.08$ Å, so that each spectral bin corresponds to the approximate FWHM spectral resolution of the RGS. At an observed wavelength of 16 Å, this equates to a resolution of $\lambda/\Delta\lambda = 200$ (or ~1500 km s^{-1} FWHM). A further binning was applied to achieve a minimum signal-to-noise ratio of 3 per bin; this ensures that the extremely low- and high-wavelength ends of the spectrum are not too noisy, in order for the continuum to be well defined. The RGS spectra were analyzed over the 6–25 Å observed wavelength range (or 5–21 Å QSO rest frame); at longer wavelengths, the spectrum is suppressed by Galactic absorption. The latter was included in the spectral fitting using the TBABS model of Wilms et al. (2000), where for PDS 456, the column density is expected to be $N_{\rm H} = 2.4 \times 10^{21}$ cm^{-2} based on 21 cm measurements (Kalberla et al. 2005). The solar abundances of Grevesse & Sauval (1998) and a conversion between energy and wavelength of 1 keV $= 1.602 \times 10^{-9}$ erg $= 12.3984$ Å were adopted.

A model consisting of a power law absorbed by the Galactic column returned a poor fit, with a reduced χ^2 of $\chi^2_\nu = 334.4/254$ and a photon index of $\Gamma = 2.71 \pm 0.09$. The RGS spectrum is plotted in Figure 2, and three possible absorption lines appear to be present against the power-law continuum. These were fitted with Gaussian profiles with rest-frame centroid wavelengths (energies) of $\lambda = 14.56 \pm 0.05$ Å (or $E = 851.8 \pm 3.5$ eV), $\lambda = 10.37 \pm 0.04$ Å ($E = 1196 \pm 5$ eV), and $\lambda = 9.30 \pm 0.06$ Å ($E = 1333 \pm 9$ eV). The line parameters are summarized in Table 2. The lines appear to be significant when added to the model; the overall fit statistic improves by $\Delta\chi^2 = -28.9$, -19.0, and -9.3, respectively, upon the addition of each line with 2 extra degrees of freedom.

We first test the scenario whereby the lines arise from a soft X-ray component of the known fast wind in PDS 456. Multiple X-ray observations of PDS 456 spanning more than a decade have shown the frequent presence of a fast outflow at iron K, with a typical velocity of $0.25c$–$0.3c$ (Reeves et al. 2009; Nardini et al. 2015; Matzeu et al. 2017a), while the possible presence of blueshifted soft X-ray features has also been noted in prior RGS spectra (Reeves et al. 2016). In this scenario, the 14.56 Å line could be identified with blueshifted O VIII Lyα (at 18.97 Å), and the derived velocity shift is then $v/c = -0.259 \pm 0.003$. Similarly, identifying the shorter-wavelength lines with the strong He and H-like ($1s \rightarrow 2p$) lines of Ne IX

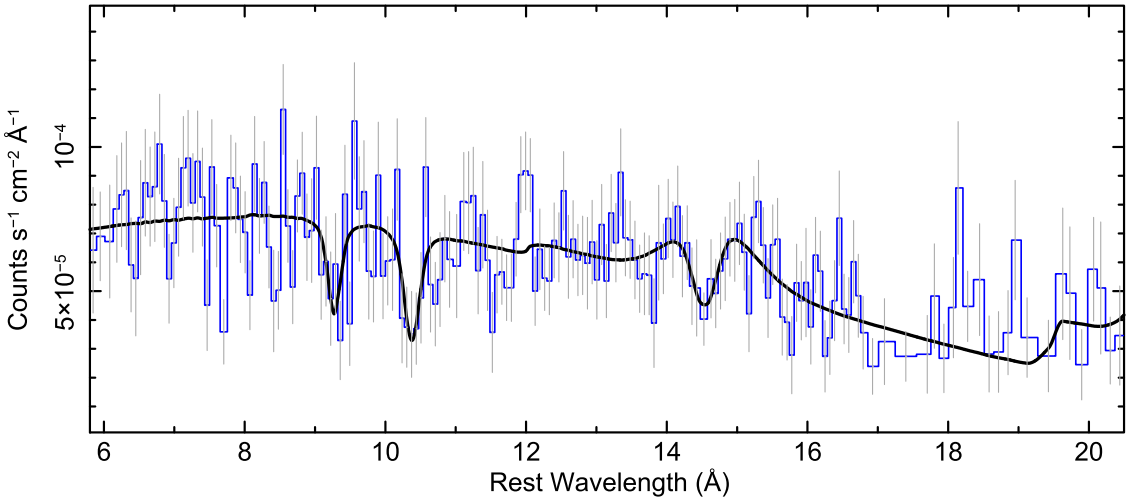

Figure 2. Count rate XMM-Newton RGS spectrum of PDS 456 from the 2019b observation, plotted in the QSO rest frame. The 1σ error bars are shown in gray. The continuum model (black line) consists of a power law (photon index $\Gamma = 2.71 \pm 0.09$) absorbed by the Galactic column. The spectrum shows three significant absorption lines modeled by Gaussian profiles centered at rest wavelengths of $\lambda = 14.56 \pm 0.05$, 10.37 ± 0.04, and 9.30 ± 0.06 Å (see Table 2). The lines could be associated with the predicted strong resonance ($1s \rightarrow 2p$) transitions of O VIII Lyα (18.97 Å), Ne IX Heα (13.45 Å), and Ne X Lyα (12.13 Å), with a common velocity shift of $v/c = -0.257 \pm 0.003$ from a fast wind. Note that the decline in flux longward of 16 Å is due to Galactic absorption.

Heα and Ne X Lyα (at lab-frame wavelengths of 13.45 and 12.13 Å) gives consistent velocity shifts, with $v/c = -0.255 \pm 0.005$ and -0.260 ± 0.009, respectively. If a common velocity shift is assumed for all three lines, then the derived outflow velocity is $v/c = -0.257 \pm 0.003$. In the following subsection, these identifications will be placed on a firmer footing based on the photoionization analysis.

Regardless of the identifications, the absorption line profiles are resolved in the RGS spectrum. A zoom-in of the three line profiles is shown in Figure 3, where each spectral bin corresponds to the FWHM resolution of the RGS gratings. Assuming a common velocity broadening across all three lines gives a velocity width of $\sigma_v = 3030^{+950}_{-740}$ km s^{-1} (or an FWHM of $\sim$7000 km s^{-1}). The velocity widths of the individual lines are also consistent within the errors if they are allowed to vary independently of each other. For the 14.56 Å line, the 1σ width is then $\Delta\lambda = 0.16^{+0.07}_{-0.05}$ Å, which corresponds to a velocity width of $\sigma_v = 3400^{+1300}_{-1000}$ km s^{-1}.

3.2. Photoionization Modeling

To provide a more physically motivated modeling of the absorber, the RGS spectrum was fitted with a grid of photoionized absorption models generated with the XSTAR code (Kallman et al. 1996). A grid was adopted for PDS 456 using the 1–1000 Ry spectral energy distribution defined in an earlier 2017 XMM-Newton observation (see Reeves et al. 2018b). Note that this earlier observation was at a similar X-ray and UV flux level to the 2019b observation, and the 1–1000 Ry ionizing luminosity was $L_{\rm ion} = 3 \times 10^{46}$ erg s^{-1}. A turbulence velocity of 3000 km s^{-1} was chosen for the grid in order to well match the widths of the absorption line profiles.

Applying the XSTAR absorption model to the RGS spectrum gave a good fit, with $\chi^2_\nu = 276.4/251$ and a corresponding improvement in the fit statistic of $\Delta\chi^2 = 58$ for $\Delta\nu = 3$ extra degrees of freedom. The column density of the absorber is $N_{\rm H} = 2.3^{+0.9}_{-0.6} \times 10^{21}$ cm^{-2}, with an ionization parameter of $\log \xi = 3.4^{+0.1}_{-0.2}$. The above fit was obtained with the elemental abundances fixed at their solar values, while the improvement in the fit was not significant when we allowed the abundances to vary with respect to the other elements (e.g., for Ne, $\Delta\chi^2 = 2.4$ for $\Delta\nu = 1$). The outflow velocity was subsequently determined from the XSTAR fit to be $v/c = -0.258 \pm 0.003$, in agreement with the simple Gaussian line analysis.

Note that the line-of-sight covering fraction of the absorber is $f_{\rm cov} = 0.92^{+0.08}_{-0.32}$; thus, the minimum covering fraction is 60%, and the model is consistent with a fully covering absorber. If the covering fraction were lower than this, then the lines would not be of sufficient depth to model the absorption profiles that are observed in the RGS spectrum.

The resulting fit to the spectrum is shown in the upper panel of Figure 4, while the lower panel shows the XSTAR model with various absorption lines marked at their expected lab-frame wavelengths prior to applying the above velocity shift. Comparing the two panels, the three strongest $1s \rightarrow 2p$ lines predicted by the model (O VIII Lyα, Ne IX Heα, and Ne X Lyα) are all systematically blueshifted by the same amount in the observed spectrum when compared to their expected lab-frame wavelengths.

3.3. Alternative Line Identifications

An identification of the lines was also attempted assuming a zero- or low-velocity shift away from their respective rest-frame wavelengths. This corresponds to the scenario whereby the lines originate from a warm absorber of modest outflow velocity (a few hundred to a few thousand km s^{-1}), as is frequently seen in the soft X-ray spectra of Seyfert 1 galaxies (Kaastra et al. 2000; Kaspi et al. 2004; Blustin et al. 2005; McKernan et al. 2007).

However, it is difficult to systematically reproduce the absorption lines without requiring the systematic blueshift. For instance, in the scenario whereby the absorber has zero or only a small velocity shift, the absorption line observed at 10.37 Å could be associated with the predicted weak $1s \rightarrow 3p$ line of Ne X Lyβ, which is expected at a lab-frame wavelength of 10.24 Å (see Figure 4, lower panel). The observed equivalent width of the 10.37 Å line is 16 ± 5 eV. However, we would then expect to observe the accompanying stronger

Table 2
Blueshifted Absorption Line Parameters to the 2019b PDS 456 Observation

ID	O VIII Lyα	Ne IX Heα	Ne X Lyα	Fe XXVI Lyα	Fe XXVI Lyα
Instrument	RGS	RGS	RGS	EPIC-pn	EPIC-pn
$\lambda_{\rm rest}$ or $E_{\rm rest}$[a]	14.56 ± 0.05 Å	10.37 ± 0.04 Å	9.30 ± 0.06 Å	8.98 ± 0.13 keV	10.2 ± 0.2 keV
EW (eV)[b]	$-11.5^{+2.9}_{-3.2}$	$-16.2^{+4.6}_{-5.3}$	$-14.0^{+5.0}_{-6.0}$	-255^{+58}_{-75}	−246 ± 70
σ(eV)[c]	$8.6^{+2.7}_{-2.1}$	12.1[f]	13.5[f]	310^{+140}_{-90}	310[g]
$\sigma_{\rm v}$ (km s^{-1})[d]	3030^{+950}_{-740}	3030[f]	3030[f]	$10{,}300^{+4700}_{-3000}$	
$\lambda_{\rm lab}$ or $E_{\rm lab}$[e]	18.97 Å	13.45 Å	12.13 Å	6.97 keV	6.97 keV
v/c[h]	−0.259 ± 0.003	−0.255 ± 0.005	−0.260 ± 0.009	−0.25 ± 0.02	−0.36 ± 0.02
$\Delta\chi^2/\Delta\nu$[i]	−28.9/3	−19.0/2	−9.4/2	−49.6/3	−30.1/2

Notes.
[a] Rest wavelength (RGS) in Å or energy (EPIC-pn) in keV of absorption line in the observed spectrum.
[b] Equivalent width of absorption line in units of eV.
[c] 1σ Gaussian width of line in units of eV.
[d] 1σ velocity width of line in units of eV.
[e] Expected lab-frame wavelength (or energy) for above line ID, with no velocity shift.
[f] Indicates line velocity width is tied with respect to that of the O VIII Lyα line (in velocity space).
[g] Indicates parameter is fixed.
[h] Blueshift of absorption line in units of c for above line ID.
[i] Improvement in fit statistic ($\Delta\chi^2$) for the addition of $\Delta\nu$ degrees of freedom to the model.

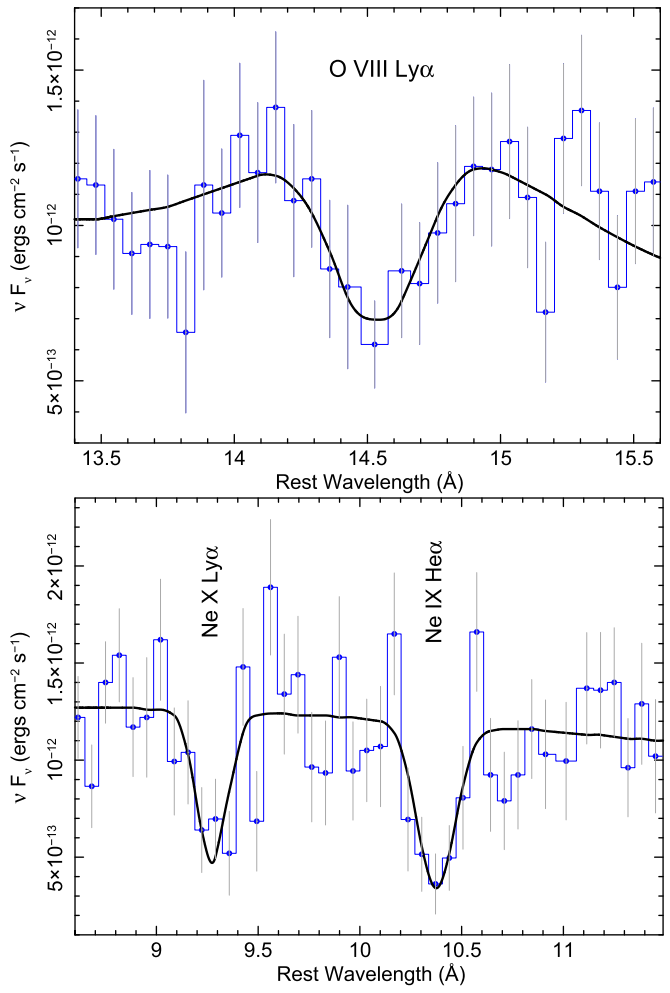

Figure 3. Zoom-in to the absorption line profiles, with the upper panel showing the putative O VIII Lyα line and the lower panel showing the $1s \rightarrow 2p$ lines from Ne IX and Ne X. The lines are all resolved by the RGS (where one bin corresponds to the FWHM resolution) and can be fitted with a common velocity width of $\sigma = 3030^{+950}_{-740}$ km s^{-1}. Note that the y-axis scale has been converted into energy units using the wavelength conversion given in the text, and both the model and data are folded through the instrumental response.

Ne X Lyα line near 12.1 Å at zero or low velocity. At this wavelength, only a tight upper limit of <2 eV can be placed on the equivalent width of any absorption line. Thus, a zero-velocity solution whereby the Ne X Lyα transition is at least 5× weaker than the corresponding Lyβ line can be physically ruled out.

Similarly, without imparting any blueshift, the observed line at 14.56 Å falls in between the expected lab wavelengths of the Fe XVII and Fe XVIII L-shell ($2p \rightarrow 3d$) transitions (at 15.01 and 14.21 Å). Both of these lines are predicted to be weaker (by a 3:1 ratio) in the model spectrum when compared to the strong O VIII Lyα line at 18.97 Å, where the latter line is a dominant transition in the photoionized absorber model (Figure 4). Instead, an upper limit of EW < 3 eV can only be placed on any 18.97 Å absorption compared to the observed line equivalent of 11.5 ± 3.0 eV at 14.56 Å. Thus, as with the above case of Ne, it appears more plausible for the O VIII Lyα line to be systematically blueshifted in order to reproduce the strong absorption profile at 14.56 Å.

To quantify this further, the XSTAR model was refitted to the spectrum, but instead forcing the outflow velocity to be within ±10,000 km s^{-1} of zero and allowing its column and ionization state to adjust. In this test, the column density drops to a very low value of $N_{\rm H} < 3.5 \times 10^{20}$ cm^{-2} (for an ionization of $\log \xi \sim 3$), the model adds little opacity to the spectrum reverting to a simple power-law continuum, and the fit statistic is subsequently worse with $\chi^2_\nu = 317.5/251$. Thus, the fast wind scenario is instead the likely preferred solution and can consistently account for the wavelengths and ratios of the observed lines in the spectrum. Furthermore, as is described below, the velocity of the iron K-band absorber is also consistent with the soft X-ray gas.

4. The Broadband Spectrum

Next, the results from the broadband X-ray spectral analysis of the 2019b observation are presented. Data from the EPIC-pn and EPIC-MOS CCD detectors were included over the 0.4–10 keV observed frame band; these have net exposures of 70.1 and 81.0 ks (after correcting for dead time) and net

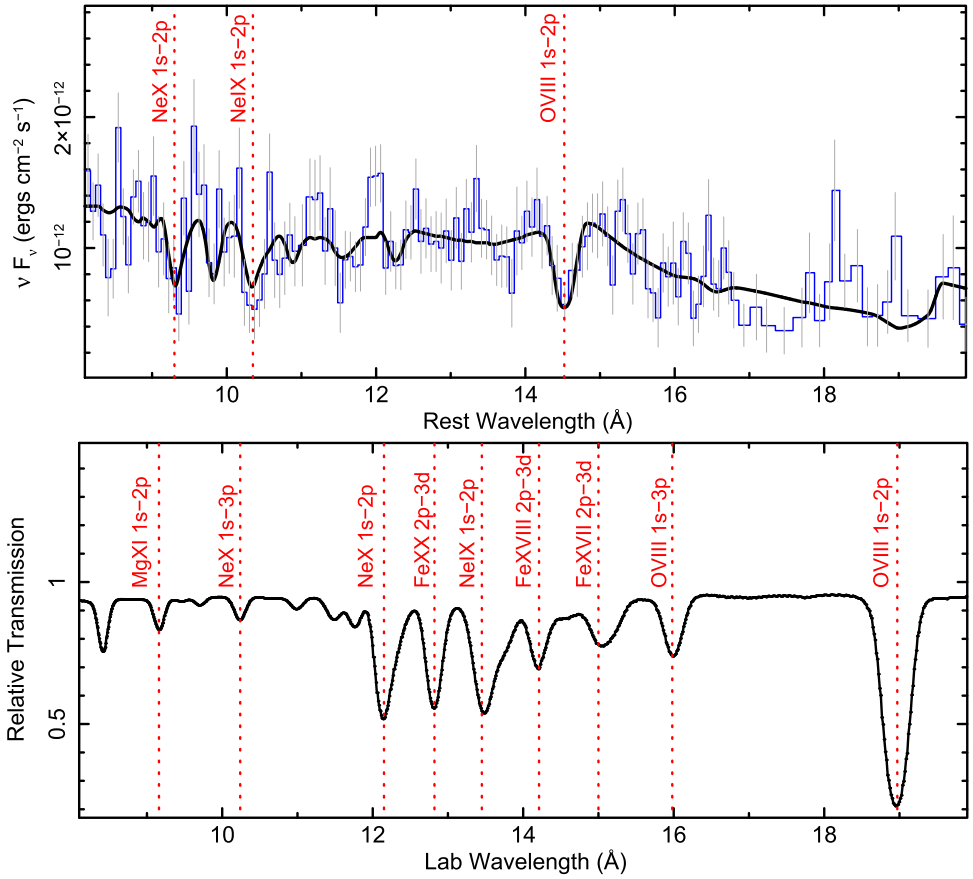

Figure 4. The XSTAR photoionization model fitted to the 2019b RGS spectrum. The upper panel shows the best-fit model overlaid on the spectrum, which well reproduces the strong $1s \rightarrow 2p$ absorption lines from O VIII Lyα, Ne IX Heα, and Ne X Lyα (as marked by dashed red lines) with a common velocity shift of $v/c = -0.258 \pm 0.003$. The lower panel shows the transmission through the same photoionized absorber without any velocity shift; i.e., the corresponding lines are at their expected lab-frame wavelengths. The blueshift of the strongest lines in the model relative to their observed positions in the upper panel is apparent. All abundances were fixed at their solar values. See text for further details.

count rates of 1.354 ± 0.004 and 0.697 ± 0.003 counts s^{-1}, respectively. The background count rate is about 1% of the source counts over the whole band and 10% of the source counts over the 7–10 keV band. Spectra from the hard X-ray NuSTAR FPMA and FPMB detectors were included in the analysis over the 3–40 keV band, with net count rates of 0.044 ± 0.001 and 0.042 ± 0.001 counts s^{-1}, respectively, while the net exposure per detector was 78.0 ks. Here the background rate is ∼10% of the source rate, although the spectrum becomes background-dominated above 40 keV. The NuSTAR observation, performed in low Earth orbit, overlapped the XMM-Newton observation, commencing just before and ending just after the XMM-Newton exposures. A constant multiplicative factor was also included between the NuSTAR and XMM-Newton spectra to allow for any cross-normalization differences between satellites; however, this was found to be consistent with 1.0 within the errors.

Per the RGS spectral analysis, a neutral Galactic absorption component of $N_{\rm H} = 2.4 \times 10^{21}$ cm^{-2} was included in the modeling. The continuum was modeled by a broken power law, which allows for the fact that the soft X-ray photon index (as seen by RGS) is somewhat steeper than at harder X-rays, due to the presence of a soft X-ray excess that is apparent once the Galactic absorber is accounted for. The continuum parameters are reported in Table 3. A high-energy exponential cutoff was also included, with an e-folding energy fixed to 50 keV. This is included for consistency with the 2018 observation, which occurred in a bright and flaring state and where the cutoff is well determined at this energy; these results will be presented in a later paper. Note that the presence of the cutoff does not affect the parameterization of the absorbers, which is our focus below.

The residuals of the pn and MOS spectra against this continuum are plotted in Figure 5 over the 0.5–12 keV rest-frame band. At higher energies, this baseline model provides an excellent description of the hard X-ray continuum as seen in NuSTAR. In the iron K band, a strong absorption line is present at a rest-frame energy of ∼9 keV, with a possible second weaker trough near 10 keV. The first line can be modeled with a Gaussian profile of centroid energy 8.98 ± 0.13 keV, a width of $\sigma = 0.31^{+0.14}_{-0.09}$ keV, and an equivalent width of -255^{+58}_{-75} eV. The addition of the line significantly improves the fit statistic by $\Delta\chi^2 = -49.6$ for a $\Delta\nu = 3$ change in degrees of freedom. Indeed, the 9 keV absorption trough has been detected in many of the previous PDS 456 observations (e.g., Reeves et al. 2009; Nardini et al. 2015; Matzeu et al. 2017a). A second line also appears to be significant against the baseline continuum ($\Delta\chi^2 = 30.1$ for $\Delta\nu = 2$), with $E = 10.2 \pm 0.2$ keV and an equivalent width of -246 ± 70 eV, while the width of the line was assumed to be the same as the 9 keV trough. For completeness, the line parameters are reported in Table 2.

The absorption features can be identified with the strong resonance lines from Fe XXV or Fe XXVI, which are frequently detected in the X-ray spectra of many nearby type I AGN

Table 3
Spectral Parameters from Photoionization Modeling to the 2019b Observation

Parameter	Value
Fe K absorber, zone 1	
$N_{\rm H} \times 10^{23}$[a]	$7.0^{+1.9}_{-1.6}$
$\log \xi$[b]	5.02 ± 0.12
v/c	-0.261 ± 0.007
$\Delta\chi^2/\Delta\nu$	$-151.8/2$
Fe K absorber, zone 2	
$N_{\rm H} \times 10^{23}$[a]	$4.1^{+3.6}_{-1.5}$
$\log \xi$[b]	5.02[j]
v/c	-0.360 ± 0.013
$\Delta\chi^2/\Delta\nu$	$-43.4/2$
Soft X-ray absorber (RGS)	
$N_{\rm H} \times 10^{21}$[a]	$2.3^{+0.9}_{-0.6}$
$\log \xi$[b]	$3.4^{+0.1}_{-0.2}$
v/c	-0.258 ± 0.003
f[c]	$0.92^{+0.08}_{-0.32}$
$\Delta\chi^2/\Delta\nu$	$-58.0/3$
Wind emission	
$N_{\rm H} \times 10^{23}$[a]	7.0[j]
$\log \xi$[b]	5.02[j]
$\kappa_{\rm xstar}$[d]	$3.0^{+0.8}_{-0.7} \times 10^{-4}$
$\Omega/4\pi$[e]	$0.53^{+0.14}_{-0.12}$
$\Delta\chi^2/\Delta\nu$	$-45.3/1$
Continuum	
$\Gamma_{\rm soft}$	2.69 ± 0.04
$\Gamma_{\rm hard}$	2.03 ± 0.03
$E_{\rm break}$[f]	1.24 ± 0.05
$N_{\rm BPL} \times 10^{-3}$[g]	1.27 ± 0.04
$L_{2-10\,\rm keV} \times 10^{44}$[h]	2.5
$L_{1-1000\rm Ry} \times 10^{46}$[i]	3.0

Notes.
[a] Units of column density $\rm cm^{-2}$.
[b] Ionization parameter (where $\xi = L/nR^2$) in units of erg cm $\rm s^{-1}$. Note that the ionization of the zone 2 iron K absorber is tied to zone 1.
[c] Covering fraction of absorber, where $f = 1$ for a fully covering absorber.
[d] Measured normalization of XSTAR emission component, where $\kappa_{\rm xstar} = f_{\rm cov} L_{38}/D^2_{\rm kpc}$ and $f_{\rm cov}$ is the emitter covering fraction ($f_{\rm cov} = \Omega/4\pi$), L_{38} is the 1–1000 Ry ionizing luminosity in units of 10^{38} erg $\rm s^{-1}$, and $D_{\rm kpc}$ is the distance to PDS 456 in units of kpc.
[e] Solid angle of the emission component ($\Omega/4\pi$), derived from the measured normalization of the emitter as above.
[f] Break energy of broken power-law continuum in units of keV. Below the break energy, the continuum has a photon index of $\Gamma_{\rm soft}$, and above the break energy, the photon index is $\Gamma_{\rm hard}$.
[g] Normalization of the broken power-law continuum component in units of photons $\rm cm^{-2}\ s^{-1}\ keV^{-1}$ at 1 keV.
[h] Absorption-corrected rest-frame 2–10 keV luminosity in units of erg $\rm s^{-1}$.
[i] Absorption-corrected ionizing luminosity calculated over the 1–1000 Ry range in units of erg $\rm s^{-1}$.
[j] Denotes parameter is tied.

(Tombesi et al. 2010; Gofford et al. 2013). For the 9 keV trough, an identification with either of the $1s \rightarrow 2p$ lines of Fe XXV Heα at 6.70 keV or Fe XXVI Lyα at 6.97 keV returns a velocity shift of $-0.28 \pm 0.02c$ or $-0.25 \pm 0.02c$. We note that the latter identification is consistent with the velocity of the soft X-ray outflow. In principle, the second 10 keV trough may be associated with the corresponding higher-order ($1s \rightarrow 3p$) lines of Fe XXV at 7.88 keV or Fe XXVI at 8.25 keV, with a resultant outflow velocity of $-0.25 \pm 0.02c$ or $-0.21 \pm 0.02c$, respectively. However, the oscillator strengths of these higher-order $1s \rightarrow 3p$ lines are typically a factor of 5 weaker than the corresponding strong $1s \rightarrow 2p$ lines, and their equivalent widths are predicted to be weaker by about the same factor. This does not appear to be the case from the observed equivalent widths reported in Table 2. Alternatively, the second higher-energy absorption trough could originate from a faster wind component, which, if it is associated with the strong Fe XXVI Lyα line, would then require a second, much higher velocity of $v/c = -0.36 \pm 0.02$. We investigate this further below in the XSTAR modeling.

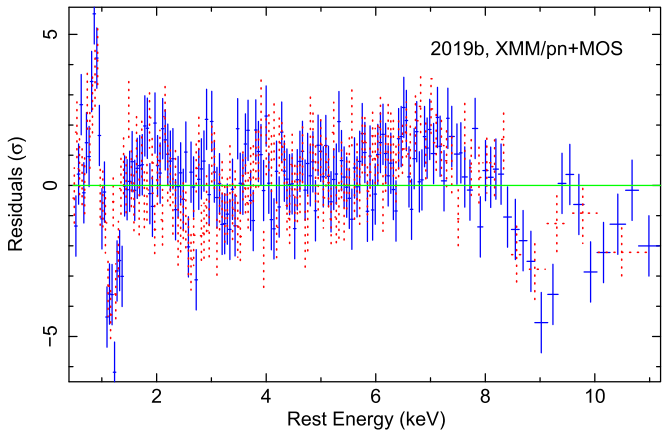

Figure 5. Residuals, plotted in terms of data–model/error, against a baseline broken power-law continuum to the broadband XMM-Newton pn (blue) and MOS (red dotted points) spectra. A strong iron K absorption trough is observed at 9 keV in the QSO rest frame, which, if it is associated with Fe XXVI Lyα at 6.97 keV, requires an outflow velocity of $v/c = -0.25 \pm 0.02$, consistent with the velocity of the soft X-ray absorber. A second trough may be present at 10.2 keV that may be either ascribed to a higher-velocity wind component or from a contribution from higher-order Fe K absorption, as described in the text. The presence of the soft X-ray trough near 1.2 keV is likely due to an unresolved blend of the Ne K-shell absorption lines, as observed in the RGS.

Interestingly, a third absorption trough is detected in the XMM-Newton spectra in the soft X-ray band at $E = 1.16 \pm 0.05$ keV (equivalent to 10.7 ± 0.4 Å); this could arise from a blend of the Ne IX–X lines seen in the RGS that is unresolved at the lower resolution of the CCD spectra.

4.1. Iron K Absorber Properties

To quantify the iron *K*-band absorption, the spectra were again modeled by XSTAR as above but adopting a grid of absorption models with a higher turbulence velocity of 10,000 km $\rm s^{-1}$ to match the widths of the lines measured from their Gaussian profiles. Emission from the wind, parameterized by a quasi-spherical distribution of gas, has also been included per the analysis of Nardini et al. (2015). Note that as detailed by Nardini et al. (2015) and Reeves et al. (2018b), the solid angle of the emitter (in terms of $f = \Omega/4\pi$) is determined by the relation $\kappa_{\rm xstar} = fL_{38}/D^2_{\rm kpc}$, where $\kappa_{\rm xstar}$ is the fitted normalization of the XSTAR emission grid, L_{38} is the 1–1000 Ry ionizing luminosity in units of 10^{38} erg $\rm s^{-1}$, and $D_{\rm kpc}$ is the distance to PDS 456 in kpc (see Table 3 for parameter details). The turbulence velocity of the emitter was fixed at 25,000 km $\rm s^{-1}$ to account for any broadening of the iron K emission, consistent with previous analysis (Nardini et al. 2015; Reeves et al. 2018b). The column density and ionization of the emitter are tied to that of the absorber, i.e., as if the emitting gas is the same matter as the

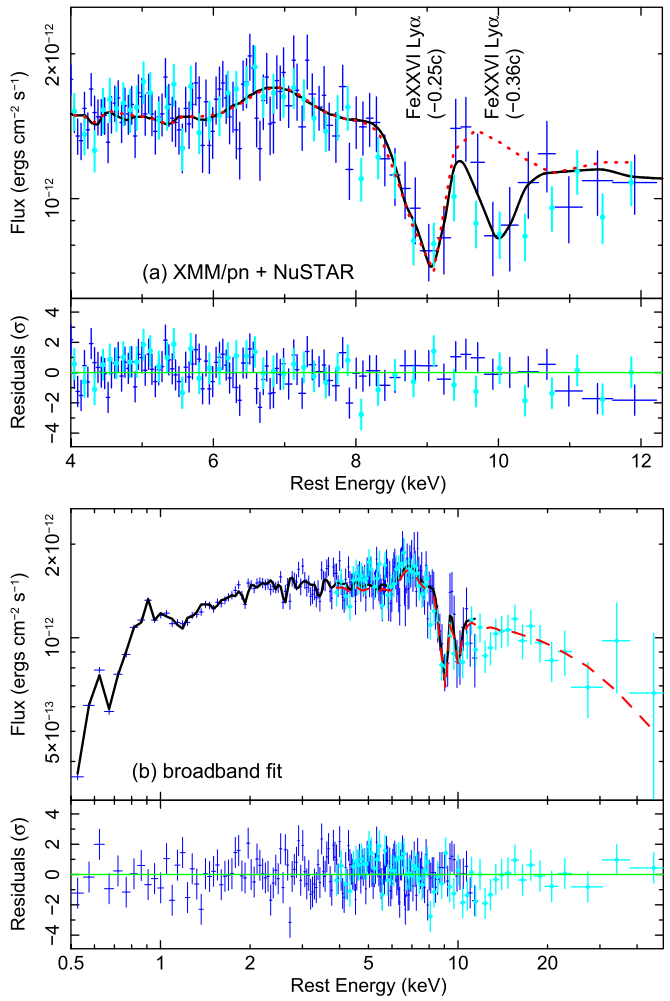

Figure 6. Best-fit photoionization model applied to the broadband XMM-Newton and NuSTAR spectra of the 2019b observation. The XMM-Newton pn spectrum is shown in blue and NuSTAR is in cyan, where for the latter, the FPMA and FPMB modules have been combined into a single spectrum. The upper panel shows a zoom-in around the iron K band, whereby a high-ionization photoionized absorber (Table 3, zone 1) can account for the 9 keV absorption trough originating from blueshifted Fe XXVI Lyα at 6.97 keV. Its outflow velocity, of $v/c = -0.261 \pm 0.007$, is consistent with the soft X-ray absorber seen in the RGS and where $v/c = -0.258 \pm 0.003$. Note that the second absorption trough near 10 keV cannot be accounted for by this zone (red dotted line) and requires the addition of a second faster wind component with $v/c = -0.360 \pm 0.013$, which can then fully model both absorption profiles (two-velocity model; solid black line). The lower panel shows the broadband spectrum and model, where the red dashed line indicates the level of the continuum as fitted to NuSTAR above 10 keV.

absorber, but integrated over a range of angles. The continuum form is as above.

The resultant fit to the XMM-Newton and NuSTAR spectra is shown in Figure 6, where the upper panel shows the zoom-in to the iron K band and the lower panel shows the whole broadband spectrum. The overall fit statistic is $\chi^2 = 416.2/365$, while the best-fit parameters of the model are summarized in Table 3. The main component (zone 1) of the Fe K absorber reproduces the 9 keV absorption trough; its outflow velocity is $v/c = -0.261 \pm 0.007$, which is in excellent agreement with the RGS absorber where $v/c = -0.258 \pm 0.003$. Note that its ionization is nearly 2 orders of magnitude higher than the soft X-ray absorber, with $\log \xi = 5.0 \pm 0.1$, while its column density is also correspondingly higher ($N_{\rm H} = 7.0^{+1.9}_{-1.6} \times 10^{23}$ cm^{-2}). At this degree of ionization, most of the opacity arises from H-like iron (e.g., Fe XXVI Lyα), and the absorber is virtually transparent at soft X-rays, with just trace amounts of absorption predicted from H-like Si and S.

As a result, the broadband spectrum also requires the addition of the soft X-ray absorber to account for the $\sim$1 keV trough. Upon using the same grid as the RGS analysis, its parameters are found to be consistent in the broadband spectrum; e.g., $N_{\rm H} = (1.4 \pm 0.2) \times 10^{21}$ cm^{-2}, $\log \xi = 3.4^{+0.3}_{-0.1}$, and $v/c = -0.25 \pm 0.02$. This reaffirms the presence of the soft X-ray absorber as measured in the RGS.

Curiously, the zone 1 iron K absorber is not able to account for the second absorption trough near 10 keV. As noted above, this is mainly because the predicted higher-order ($1s \rightarrow 3p$) lines of iron are much weaker and make a negligible contribution toward the absorption trough. This is illustrated in the upper panel of Figure 6, where the red dashed line represents an XSTAR model with only one velocity component (at $-0.25c$) that is not able to model the second higher-energy trough. Instead, a second Fe K absorption zone of higher velocity is required, with $v/c = -0.360 \pm 0.013c$ (zone 2, as listed in Table 3), which improves the fit statistic further by $\Delta\chi^2 = -43.4$ for $\Delta\nu = 2$ and is able to model the 10 keV profile (see Figure 6, solid black line, for the two-velocity solution). Note that the ionization has been assumed to be the same as that of zone 1. At this velocity, the 10 keV trough corresponds to a second velocity component of Fe XXVI Lyα, perhaps arising from a faster streamline of the wind. Note that the presence of more complex velocity structure at Fe K has been noted in other observations of PDS 456 (Reeves et al. 2009, 2018a) and may also be present toward other AGN, e.g., PG 1211+143 (Pounds et al. 2016), APM 08279+5255 (Chartas et al. 2009), and MCG−03−58−007 (Braito et al. 2018).

5. Discussion

A new observation of PDS 456 from 2019 September was presented that revealed three resolved lines in the soft X-ray spectrum taken with the XMM-Newton RGS. The lines are required to originate from a fast outflowing absorber that, when fitted with XSTAR, was found to have an outflow velocity of $v/c = -0.258 \pm 0.003$, with the lines originating from the $1s - 2p$ transitions of O VIII Lyα, Ne IX Heα, and Ne X Lyα. The outflow velocity of the soft X-ray absorber is entirely consistent with the main zone of iron K absorption, confirmed from the same data set, which has an outflow velocity of $v/c = -0.261 \pm 0.007$.

This observation of PDS 456 represents one of the small but growing number of cases where the velocity of the ultrafast outflow, as first detected in the iron K band, has been confirmed by an analysis of a grating resolution spectrum in the soft X-ray band (e.g., Pounds et al. 2003; Parker et al. 2017; Kosec et al. 2018; Pinto et al. 2018). Indeed, one of the first known objects for the presence of a fast wind, the nearby ($z = 0.0809$) QSO PG 1211+143 (Pounds et al. 2003), also simultaneously shows the presence of both a soft X-ray and iron K wind, with a self-consistent velocity. The presence of the soft X-ray wind in PG 1211+143, with a velocity of $v/c = -0.06$, was recently confirmed through deep observations with both the XMM-Newton RGS and Chandra HETG gratings (Danehkar et al. 2018; Reeves et al. 2018). This velocity was also consistent with the major component of the iron K absorption

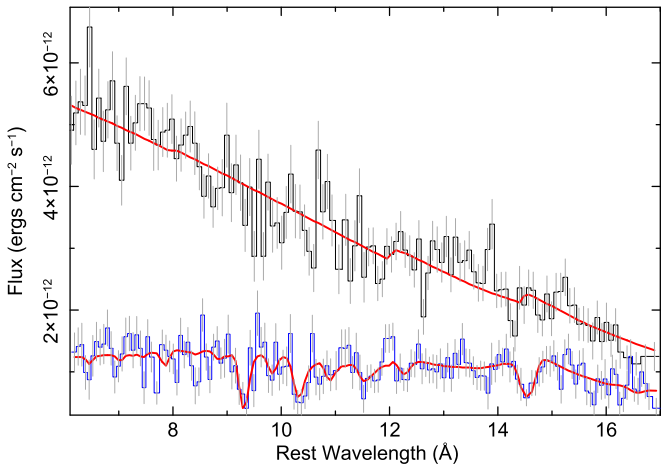

Figure 7. Comparison between the bright 2018 RGS spectrum of PDS 456 (black line) and the lower-flux 2019b spectrum (blue line), with the best-fit XSTAR model overlaid for the latter (red line). With respect to the 2019b observation, the flux of the 2018 spectrum was a factor of 4 brighter in both the soft band and the harder 2–10 keV band. The 2018 spectrum appears featureless, fitted by a power law of $\Gamma = 1.90 \pm 0.04$ modified by Galactic absorption, and no significant absorption features are apparent close to the wavelengths of the absorption lines detected in the 2019 spectrum. The difference could be reconciled by the subsequent increase in flux that occurred during the 2018 observation, leading to at least a factor of 4 increase in gas ionization. This is sufficient to render the 2018 spectrum featureless.

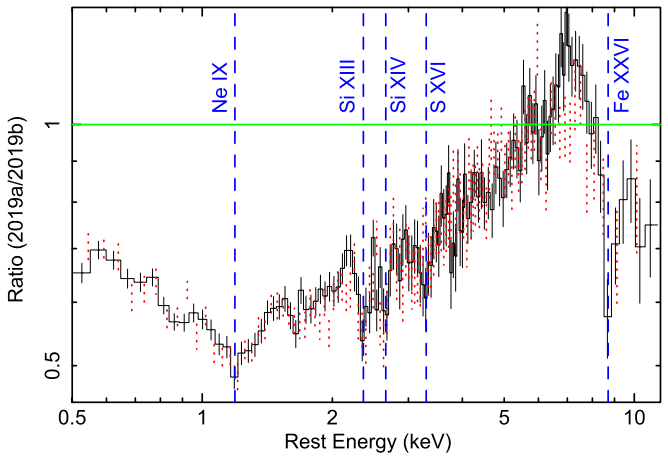

Figure 8. The 2019a XMM-Newton spectrum of PDS 456, plotted as a ratio to the continuum model defined in the 2019b observation in Table 3, where the pn is shown in black and MOS in red. Compared to the 2019b observation, the 2019a spectrum is much more strongly absorbed in the soft X-ray band and requires a high column density ($N_{\rm H} \sim 10^{23}$ cm^{-2}), low-ionization ($\log \xi = 2$) absorber to account for the strong bound-free absorption opacity present. Per the 2019b observation (Figure 5), a deep iron K absorption line is present near 9 keV, with an outflow velocity of $v/c = -0.245 \pm 0.010$. Note that dashed vertical lines represent the possible absorption line structure present in the spectrum from He/H-like Ne, Si, S, and Fe.

(Pounds et al. 2016), as well as with the broad Lyα absorption trough as observed from HST/COS spectroscopy (Kriss et al. 2018).

Another notable example, illustrating the coexistence of both soft X-ray and Fe K components of a fast wind, occurs in the NLS1, IRAS 13224−3809 (at $z = 0.0658$), where the ultrafast outflow also has a typical velocity of $-0.24c$ (Parker et al. 2017; Pinto et al. 2018). Interestingly, from a refined analysis of this AGN, Chartas & Canas (2018) found a positive correlation between the outflow velocity and X-ray luminosity, similar to the behavior previously seen in PDS 456 (Matzeu et al. 2017a) and APM 08279+5255 (Saez & Chartas 2011), that advocated for the effect of radiation pressure on the wind.

5.1. Comparison with Previous PDS 456 Observations

5.1.1. Comparison with 2018

The soft X-ray outflows in both PG 1211+143 (Reeves et al. 2018) and IRAS 13224−3809 (Pinto et al. 2018) show pronounced variability, with the outflow opacity generally being higher when the source flux is lower. In the above analyses, this was attributed to variations in either ionization versus flux, intrinsic variability of the absorber column, or a combination of both. For PDS 456, the bright 2018 observation performed 1 yr before the 2019b observation provides a test case to see how the soft X-ray absorber varies with flux. The observed soft X-ray flux in 2018 was $F_{0.4-2.0\,\rm keV} = 4.8 \times 10^{-12}$ erg cm^{-2} s^{-1} compared to $F_{0.4-2.0\,\rm keV} = 1.5 \times 10^{-12}$ erg cm^{-2} s^{-1} in the fainter 2019b observation. Note that in the 2–10 keV band, there is a factor of 4 difference in flux between observations (see Table 1). Figure 7 shows the 2018 RGS spectrum with the 2019b spectrum overlaid on the same flux scale. In contrast to the 2019b spectrum, the 2018 observation is dominated by a bright power-law component with a harder photon index of $\Gamma = 1.90 \pm 0.04$ and no soft excess compared to the 2–10 keV band, while there are no absorption features apparent in the spectrum.

To reconcile this difference, the 2018 spectrum was fitted with the same soft X-ray absorption model as in Section 3.2, allowing only the ionization parameter to adjust between the 2018 and 2019b epochs. Subsequently, for the same column density, the wind ionization decreased by at least a factor of 4 between the 2018 and 2019b spectra, in line with the continuum change, i.e., $\log \xi > 3.8$ (in 2018) to $\log \xi = 3.3^{+0.1}_{-0.2}$ (in 2019b). Per the above AGN, the featureless nature of the bright 2018 observation is consistent with the wind ionization responding to the continuum flux. Note that the change in opacity could be equally expressed in terms of the equivalent factor of 4 change in column density (for a constant ionization), where $N_{\rm H} < 3.5 \times 10^{20}$ cm^{-2} in 2018.

5.1.2. Comparison with 2019a

The 2019b spectrum can also be compared to the 2019a observation that occurred 22 days prior in 2019 September (see Table 1). As can be seen from Figure 1, its soft X-ray flux was substantially lower (with $F_{0.4-2.0\,\rm keV} = 9.0 \times 10^{-13}$ erg cm s^{-1}). In contrast to the 2018 observation, it represents one of the lowest flux observations of PDS 456; it is comparable to the low-flux state observed with Suzaku in 2013 (Matzeu et al. 2016).

The 2019a spectrum is also shown in Figure 8, where it has been replotted as a ratio of the best-fit continuum model defined from the 2019b observation. Per the 2019b observation, a strong absorption trough is present in the Fe K-shell band near 9 keV and is characterized by a fast, high-ionization wind with very similar parameters, where $N_{\rm H} = 5.0^{+1.4}_{-1.1} \times 10^{23}$ cm^{-2}, $\log \xi = 5.0 \pm 0.2$, and $v/c = -0.245 \pm 0.010$. In contrast, the 2019a spectrum is much more strongly absorbed in the soft X-ray band, requiring a higher column density of $N_{\rm H} = 1.24^{+0.08}_{-0.11} \times 10^{23}$ cm^{-2}, while its ionization is low, with $\log \xi = 2.0 \pm 0.1$. The covering fraction of the absorber, against a best-fit power-law continuum of photon index $\Gamma = 2.37 \pm 0.03$, is found to be $f_{\rm cov} = 0.77 \pm 0.02$, while the velocity of the soft X-ray absorber

Table 4
Absorption Parameters from the 2019a Observation

Parameter	Value
Fe K absorber	
$N_{\rm H} \times 10^{23}$[a]	$5.0^{+1.4}_{-1.1}$
$\log \xi$[b]	5.0 ± 0.2
v/c	-0.245 ± 0.010
$\Delta\chi^2/\Delta\nu$	$-63.0/3$
Soft X-ray absorber	
$N_{\rm H} \times 10^{23}$[a]	$1.24^{+0.08}_{-0.11}$
$\log \xi$[b]	2.0 ± 0.1
v/c	-0.257 ± 0.015
f[c]	0.77 ± 0.02
$\Delta\chi^2/\Delta\nu$	$-288.9/4$

Notes.
[a] Units of column density $\rm cm^{-2}$.
[b] Ionization parameter (where $\xi = L/nR^2$) in units of erg cm $\rm s^{-1}$.
[c] Covering fraction of absorber, where $f = 1$ for a fully covering absorber.

is measured to be $v/c = -0.257 \pm 0.015$. The absorption properties of the 2019a observation are summarized in Table 4. The fit statistic with this model is good, with $\chi^2_\nu = 297.8/302$.

Although the 2019a observation is dominated by the strong bound-free continuum opacity produced by the high-column soft X-ray absorber, there are some indications of absorption line structure in the soft X-ray spectrum plotted in Figure 8 (dashed blue vertical lines). In particular, a pronounced trough at 1.2 keV is observed at the same energy as the 2019b spectrum. This could also coincide with the Ne IX–X absorption blend shifted by $-0.25c$ or some additional contribution from Fe L-shell absorption. There are also indications of absorption structures between 2 and 3.5 keV, which may be consistent with blueshifted absorption from He and H-like Si and S.

To investigate this further, we compared the above partially ionized soft X-ray absorber with an alternative neutral partial covering absorber (using the ZPCFABS model within XSPEC), where the outflow velocity is assumed to be zero in the latter model. In both cases, we retain the highly ionized iron K wind component in absorption and emission, which reproduces the prominent P Cygni–like feature seen at high energies. While the neutral absorber has a similar column density to the ionized one ($N_{\rm H} = 1.27^{+0.17}_{-0.14} \times 10^{23}$ $\rm cm^{-2}$ for a covering fraction of $f_{\rm cov} = 0.48 \pm 0.05$), it fails to reproduce the overall shape of the spectrum. Figure 9 (left panel) shows the comparison between the ionized and neutral absorbers. Significant residuals are present against the neutral absorber, in particular a broad emission and absorption trough near 1 keV, and the fit statistic is very poor, with $\chi^2_\nu = 494.0/304$. In contrast, the ionized absorber is able to account for these soft X-ray residuals, chiefly from the interplay between ionized absorption and emission produced from the outflowing gas.

Note that the outflow velocity derived from the ionized soft X-ray absorber, $v/c = -0.257 \pm 0.015$, is fully consistent with both the Fe K-band absorber and the soft X-ray absorber seen toward the 2019b spectrum. Statistically speaking, the outflow velocity of the soft X-ray absorber is well determined, as is illustrated in the right panel of Figure 9, whereby a lower-velocity solution is ruled out with a high degree of confidence (e.g., $\Delta\chi^2 > 80$ for zero outflow velocity). Nonetheless, the exact velocity determination should be treated with some caution, as the strong spectral curvature toward the 2019a spectrum and its lower resolution precludes a detailed line-by-line analysis, unlike for the 2019b spectrum. In the future, high-resolution calorimeter-based spectroscopy with XRISM and ATHENA will be able to provide detailed measurements of these obscuration events.

Overall, the low-ionization, high-column absorber in the 2019a observation produces substantial bound-free opacity and, as a result, suppresses the continuum toward low energies with only a fraction (about 20%) of the direct continuum emerging in the soft band. Its effect on the X-ray continuum is similar to what was recently observed in other Seyfert 1s, such as NGC 5548 (Kaastra et al. 2014), NGC 3783 (Mehdipour et al. 2017), and Mrk 335 (Longinotti et al. 2019; Parker et al. 2019), where these AGN have undergone an X-ray obscuration event, substantially suppressing the soft X-ray flux. In all of these examples, broad and blueshifted UV absorption line profiles also accompanied the increased X-ray absorption (e.g., Kriss et al. 2019), linking the obscuration to the emergence of an outflow. The obscuration duration can be prolonged, lasting years in the cases of NGC 5548 and Mrk 335. In PDS 456, this timescale is likely much shorter, lasting no longer than the 20 day interval between the two 2019 XMM-Newton observations. Indeed, similar short-lived X-ray obscuration events, of the order of days, have also been observed in the Seyfert 1 NGC 3227 (Turner et al. 2018) and the QSO PG 1211+143 (Reeves et al. 2018). In the latter AGN, the obscuration was also attributed to an order-of-magnitude increase in the column of the lower-ionization but fast soft X-ray wind.

5.1.3. Comparison with Earlier Observations

There have also been multiple observations of PDS 456 with XMM-Newton prior to the current campaign. These were performed in 2001 (Reeves et al. 2003), 2007 (Behar et al. 2010), 2013–2014 (five observations; Nardini et al. 2015; Reeves et al. 2016), and 2017 (Reeves et al. 2018a, 2018b). While a systematic analysis of all of the RGS spectra is beyond the scope of the current paper, a general comparison can be made with these published observations compared to the present epoch. In particular, Reeves et al. (2016) analyzed all of the archival RGS spectra from 2001 to 2014. Several of these spectra showed a pronounced broad absorption trough around 1.2 keV or in the typical wavelength range from 10 to 12 Å. This was attributed to a blend of absorption lines arising from Ne IX–X and L-shell iron, similar to what is also predicted here, with an outflow velocity in the range between $0.17c$ and $0.27c$, column densities of up to 10^{22} $\rm cm^{-2}$, and ionization parameters of about $\log \xi \sim 3.5$–4. Indeed, the soft X-ray absorber parameters measured in the 2019b observation are similar to these values, but the column toward PDS 456 during the low-flux 2019a observation is much higher.

One major difference with 2019b when compared to some of these earlier observations is that the 1.2 keV absorption trough appeared much broader previously. For example, in the third and fourth observations of the 2013–2014 campaign (OBS CD; Reeves et al. 2016), its velocity width was $\sigma = 28{,}000^{+13{,}000}_{-9000}$ $\rm km\,s^{-1}$. As a result, it was not possible to resolve the earlier absorption profiles into a distinct series of absorption lines. This has only been achieved in the current 2019b epoch, as the line widths are much narrower, $\sigma = 3000$ $\rm km\,s^{-1}$, which may indicate a decrease in the turbulence velocity arising from the

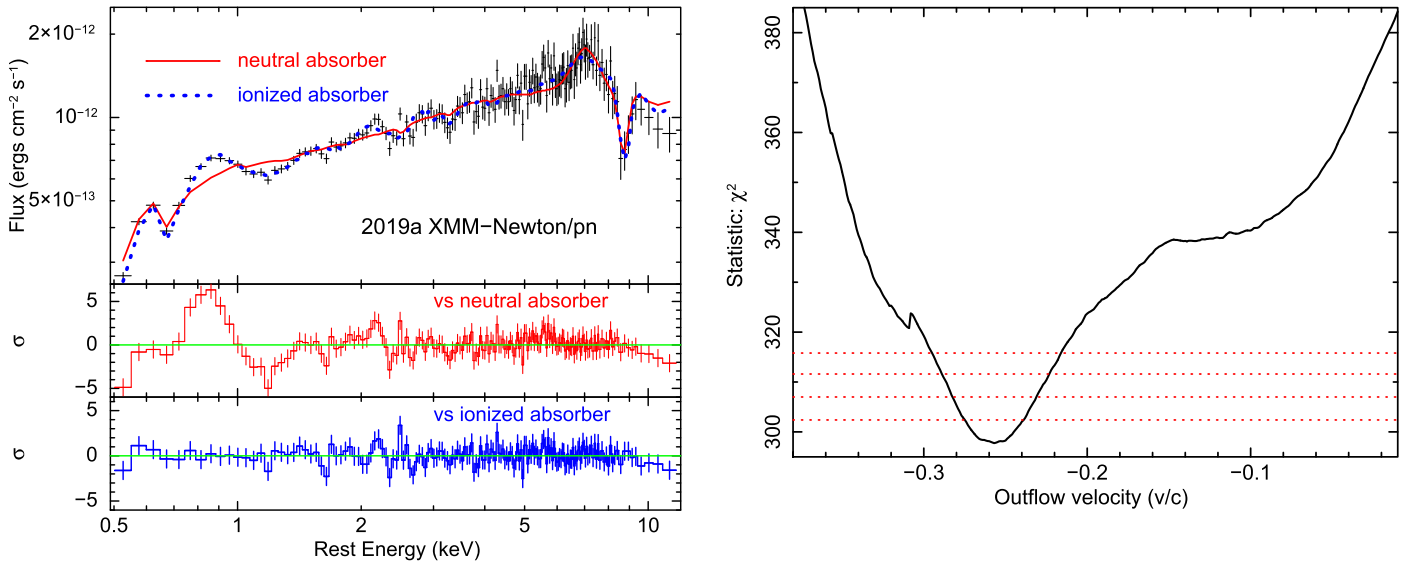

Figure 9. Left panel: 2019a low-flux spectrum compared to either a neutral or a partially ionized soft X-ray absorber. The top panel shows the models overlaid on the data, where the solid red line corresponds to the neutral absorber and the dotted blue line is the ionized absorber. The P Cygni–like profile in the iron *K* band is included in both cases. The lower panels show the residuals against these two models. Significant soft X-ray residuals are seen against the neutral absorber, which the ionized absorber can account for via a soft X-ray wind. Right panel: fit statistic as a function of outflow velocity for the ionized absorber in the 2019a spectrum, where the dotted horizontal lines correspond to the 90%, 99%, 99.9%, and 99.99% confidence levels for two interesting parameters. The best-fit outflow velocity is $v/c = -0.257 \pm 0.015$, while a lower-velocity solution is formally excluded.

passage of a different streamline across the line of sight. As a result, it was possible in the new 2019b data to both resolve and identify the discrete soft X-ray absorption lines and to confirm that the velocity of both the soft X-ray and iron K absorbers are identical.

5.2. The Origin of the Soft X-Ray Wind

The major difference between the soft X-ray and iron K wind components in PDS 456 is that the former has a much lower ionization, by about 2 orders of magnitude, compared to the latter. Thus, can the soft X-ray absorber exist cospatially with the inner high-ionization Fe K-shell wind, or does it have a separate origin? We have also observed the soft X-ray wind column to decrease by almost two orders of magnitude in the 20 days between the 2019a and 2019b observations ($N_{\rm H} = 10^{23}$ to 2×10^{21} cm^{-2}), while its ionization also increased by a factor of 10 (from $\log \xi \sim 2$ to 3). This is in contrast to the high-ionization wind, which remains stable in both column and ionization during this period. Thus, at first sight, this suggests that the soft X-ray absorber is clumpy, while the high-ionization gas is relatively homogeneous.

We first consider the soft X-ray absorber as measured in the 2019b observation. Given that this absorber has a minimum covering fraction toward the X-ray source of 60% (and is consistent with a fully covering absorber), its size scale must be at least similar to the X-ray source size (if not larger). For PDS 456, the X-ray coronal size has been previously estimated to be of the order of $\sim 10^{15}$ cm (or $\sim 10 R_{\rm g}$ for a black hole mass of $10^9\,M_{\odot}$), as measured from X-ray flares (Reeves et al. 2002, 2018b; Matzeu et al. 2016, 2017b). Thus, to achieve a high line-of-sight coverage, the minimum absorber size scale is $\Delta R \sim 10^{15}$ cm, while for a column of $N_{\rm H} \approx 10^{21}$ cm^{-2}, the maximum absorber density is $n = N_{\rm H}/\Delta R \sim 10^6$ cm^{-3}. Thus, for an ionizing luminosity of $L_{\rm ion} = 3 \times 10^{46}$ erg s^{-1}, an ionization parameter of $\log \xi = 3.4$ and as $R^2 = L_{\rm ion}/\xi n$, this yields a minimum radial distance estimate of about 1 pc. This is also consistent with what was estimated in Reeves et al. (2016) for the soft X-ray absorber based on the previous RGS observations of PDS 456.

Alternatively, if the soft X-ray absorber were located closer in, at a similar distance to the high-ionization wind, then it would be far too compact. At a distance of $R \sim 10^{16}$ cm (or $10^2 R_{\rm g}$), coincident with the expected launching point of the inner iron K disk wind inferred by Nardini et al. (2015), the soft X-ray absorber density is required to be high ($n \sim 10^{11}$ cm^{-3}) in order to maintain its lower ionization. As a result, its size scale would then be implausibly small ($\Delta R = N_{\rm H}/n \sim 10^{10}$ cm). In contrast, placing the high-ionization absorber at this radius (with $\log \xi = 5$, $N_{\rm H} = 10^{24}$ cm^{-2}) yields a much more plausible density and size scale, where $n \sim 10^9$ cm^{-3} and $\Delta R \sim 10^{15}$ cm. Thus, it appears unlikely that the soft X-ray wind can be cospatial with the innermost disk wind.

In the 2019a observation, the column of the soft X-ray absorber was much higher at $N_{\rm H} = 10^{23}$ cm^{-2}, and its ionization was lower at $\log \xi = 2$. As above, in order to achieve a large ~80% line-of-sight coverage (Table 4), its size scale must be at least similar to the X-ray source, where $\Delta R \sim 10^{15}$ cm. In this instance, the implied density is $n \sim 10^8$ cm^{-3}; thus, the derived distance is $R \sim 10^{18}$ cm, i.e., again of the order of 1 pc. The timescale of the absorber variability also gives an indication of its size scale. The absorber variations from 2019a to 2019b occur within a timescale of 1–20 days—i.e., the minimum duration is at least as long as the 2019a XMM-Newton observation—while the absorption has declined by the onset of the 2019b observation. If the absorption changes are due to gas moving across our line of sight, then for a maximum transverse cloud velocity of $v = 0.25c$, the absorber size scale is constrained to within $\Delta R = v\Delta t \sim 10^{15}$–$10^{16}$ cm, consistent with the above. Note that the Swift light curve may indicate that the duration of the obscuration event is confined to a few days; thus, ΔR is at the lower end of the range if it is coincident with the period of low flux at the start of the X-ray monitoring.

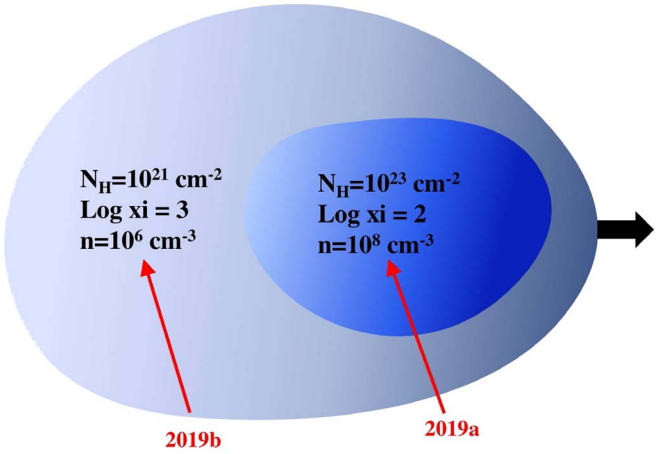

Figure 10. Possible geometry of the soft X-ray absorber responsible for the variation in column between the 2019a and 2019b observations. The red arrows represent our view toward the absorber for the 2019a and 2019b observations, and the thick black arrow is the direction of the cloud. During the 2019a observation, our sight line intercepts a denser, higher-column (10^{23} cm^{-2}) part of the absorber (dark blue), while in 2019b, the absorption has decreased, as we now view through lower density and lower column gas (light blue). Note that the maximum size scale of the absorber is set by the 20 day timescale between observations ($\Delta R \sim 10^{16}$ cm), while to maintain its lower ionization, the absorber is likely located on parsec scales.

The soft X-ray absorption seen toward both the 2019a and 2019b observations is consistent with being at a similar location; they have the same velocity and may form part of the same streamline, which has a density (and ionization) gradient across the flow. A possible geometry for the absorbing cloud, which may form part of an ensemble, is shown in Figure 10. Thus, during the heavily obscured 2019a epoch, we are intercepting a denser, higher-column portion of the absorber, while 20 days later, we are instead viewing through a lower-density and more ionized tail of the absorber. This may be similar to what was envisaged by Maiolino et al. (2010), where elongated cometary-shaped clouds may be responsible for the short-timescale column density and covering fraction variations seen toward the changing-look Seyfert NGC 1365. Alternatively, a scenario whereby more compact, higher-density clouds can intercept the line of sight in front of the lower-density gas may also be possible.

In PDS 456, the clumpy, lower-ionization soft X-ray absorbing clouds likely form from gas further out (on parsec scales) compared to the highest ionization phase of the disk wind, which is launched closer to the black hole. A similar scenario was postulated by Serafinelli et al. (2019) for PG 1114+445, whereby a possible fast soft X-ray absorber originates from clouds entrained within the high-ionization ultrafast outflow.

We can consider further the mass outflow rate of the soft X-ray wind and the subsequent geometric covering fraction ($f_{\rm cov} = \Omega/4\pi$) and volume filling factor ($f_{\rm v}$) of the gas. Taking an expression for the mass outflow rate ($\dot{M}_{\rm out}$) that accounts for the covering and filling factors of the gas (e.g., Blustin et al. 2005),

$$\dot{M}_{\rm out} \approx 4\pi f_{\rm cov} f_{\rm v} \mu m_{\rm p} v_{\rm out} n R^2, \quad (1)$$

where $\mu = 1.3$ for solar abundances and $nR^2 = L_{\rm ion}/\xi$ from the definition of the ionization parameter. For the soft X-ray wind in PDS 456, where $L_{\rm ion} = 3 \times 10^{46}$ erg s^{-1} and $\log \xi = 3.4$, the product $nR^2 = 10^{43}$ cm^{-1}, while $v_{\rm out} = 0.25c$. Thus, the soft X-ray mass outflow rate is $\dot{M}_{\rm out} \approx 10^4 f_{\rm cov} f_{\rm v}\, M_\odot$ yr^{-1}. This seems implausibly high for a homogeneous outflow where $f_{\rm v} \sim 1$ and would easily exceed the expected mass accretion rate for PDS 456.

In contrast, for the innermost high-ionization ($\log \xi = 5$) iron K wind component originating from close to the launch radius ($R \sim 100 R_{\rm g}$ or $\sim 10^{16}$ cm), Nardini et al. (2015) derived a mass outflow rate of $\dot{M}_{\rm out} \approx 10\, M_\odot$ yr^{-1}. Such highly ionized gas is likely to be more homogeneous in nature (i.e., $f_v \sim 1$), while Nardini et al. (2015) derived a high geometric covering factor for the gas of $f_{\rm cov} \sim 0.5$, as measured by its iron K-shell P Cygni profile. Instead, while the soft X-ray mass outflow rate cannot be reliably estimated per se, the above argument supports the hypothesis whereby this gas is highly clumped, where its volume filling factor is likely to be at least $f_{\rm v} = 10^{-3}$. This is also consistent with the above size scales and radial distance for the soft X-ray absorber, where one would typically estimate that $\Delta R/R \sim 10^{-3}$.

Interestingly, the heavily obscured 2019a XMM-Newton observation commenced just 2 days prior to an observation with HST/COS, where the aim of the latter was to measure the properties of any UV outflow toward PDS 456 and its relation to the X-ray wind. Indeed, the high column density ($N_{\rm H} = 10^{23}$ cm^{-2}) and low ionization ($\log \xi = 2$) of the X-ray absorbing gas should leave its imprint on the UV spectrum, producing broad absorption lines such as from C IV, as has also been discussed by Hamann et al. (2018) for PDS 456. The depth of any such UV troughs would critically depend on the geometry and covering factor of the absorbing clouds relative to a more extended UV continuum source compared to the compact X-ray corona. For instance, if the clouds are relatively compact (i.e., $\Delta R \sim 10^{15}$ cm) and have a low filling factor, then they may only obscure a small portion of the near-UV continuum. Future work (F. Hamann et al. 2020, in preparation) will quantify the presence of any UV absorption toward PDS 456 during the 2019a epoch and the implications for the properties of the obscuring gas.

In feedback scenarios, such as those suggested by King (2010), the soft X-ray absorber may arise from the slower postshock gas resulting from the interaction of the inner ultrafast outflow with the surrounding ambient interstellar medium (ISM). This was suggested to be a possible origin of the soft X-ray wind in IRAS 17020+4544 (Longinotti et al. 2015), where in particular, the complex velocity behavior of the slower warm absorbing gas may result from the interaction of the wind with the ambient ISM (Sanfrutos et al. 2018). Likewise, in NGC 4051, a wealth of absorption lines with velocity components of up to $\sim -10{,}000$ km s^{-1} were detected (Pounds & Vaughan 2011) and interpreted as originating from a cooling shocked flow (Pounds & King 2013). However, this cannot be the case in PDS 456, as the soft X-ray clouds have the same velocity as the Fe K-shell wind and are continuing to coast at the terminal velocity of $-0.25c$.

A low filling factor of the clumpy soft X-ray gas could also impact the efficiency of the X-ray wind for imparting energy-conserving feedback on larger scales. For instance, from the CO observations of PDS 456 obtained from the Atacama Large Millimeter/submillimeter Array, Bischetti et al. (2019) showed that the kinetic power of the larger-scale molecular outflow is likely much lower than the inner X-ray wind by a typical factor of 10^{-2}–10^{-3}. In principle, the inhomogeneous nature of the X-ray wind may account for the relatively low efficiency factor

both in this and toward other AGN (Fiore et al. 2017; Bischetti et al. 2019; Reeves & Braito 2019; Sirressi et al. 2019).

J.R. acknowledges financial support through grants 80NSSC18K1603 and HST-GO-14477. V.B. acknowledges support from grant No. GO7-18091X. V.B. and J.R. both acknowledge support from grant 80NSSC20K0793. E.N. acknowledges a financial contribution from agreement ASI-INAF No. 2017-14-H.0 and partial support from EU Horizon 2020 Marie Skłodowska-Curie grant agreement No. 664931. F.H. acknowledges support from the Hubble Space Telescope guest observer program HST-GO-15309. Based on observations obtained with XMM-Newton, an ESA science mission with instruments and contributions directly funded by ESA member states and NASA.

ORCID iDs

J. N. Reeves https://orcid.org/0000-0003-3221-6765
V. Braito https://orcid.org/0000-0002-2629-4989
G. Chartas https://orcid.org/0000-0003-1697-6596
S. Laha https://orcid.org/0000-0002-2002-6350
E. Nardini https://orcid.org/0000-0001-9226-8992

References

Behar, E., Kaspi, S., Reeves, J., et al. 2010, ApJ, 712, 26
Bischetti, M., Piconcelli, E., Feruglio, C., et al. 2019, A&A, 628, A118
Blustin, A. J., Page, M. J., Fuerst, S. V., et al. 2005, A&A, 431, 111
Boissay-Malaquin, R., Danehkar, A., Marshall, H. L., et al. 2019, ApJ, 873, 29
Braito, V., Reeves, J. N., Matzeu, G. A., et al. 2018, MNRAS, 479, 3592
Chartas, G., Brandt, W. N., Gallagher, S. C., & Garmire, G. P. 2002, ApJ, 579, 169
Chartas, G., & Canas, M. H. 2018, ApJ, 867, 103
Chartas, G., Saez, C., Brandt, W. N., Giustini, M., & Garmire, G. P. 2009, ApJ, 706, 644
Crenshaw, M. D., Kraemer, S. B., & George, I. M. 2003, ARA&A, 41, 117
Danehkar, A., Nowak, M. A., Lee, J. C., et al. 2018, ApJ, 853, 165
den Herder, J. W., Brinkman, A. C., Kahn, S. M., et al. 2001, A&A, 365, L7
Ferrarese, L., & Merritt, D. 2000, ApJ, 539, 9
Fiore, F., Feruglio, C., Shankar, F., et al. 2017, A&A, 601, A143
Gebhardt, K. 2000, ApJ, 539, 13
Gofford, J., Reeves, J. N., Braito, V., et al. 2014, ApJ, 784, 77
Gofford, J., Reeves, J. N., McLaughlin, D. E., et al. 2015, MNRAS, 451, 4169
Gofford, J., Reeves, J. N., Tombesi, F., et al. 2013, MNRAS, 430, 60
Grevesse, N., & Sauval, A. J. 1998, SSRv, 85, 161
Gupta, A., Mathur, S., & Krongold, Y. 2015, ApJ, 798, 4
Gupta, A., Mathur, S., Krongold, Y., & Nicastro, F. 2013, ApJ, 772, 66
Hagino, K., Odaka, H., Done, C., et al. 2015, MNRAS, 446, 663
Hamann, F., Chartas, G., Reeves, J., et al. 2018, MNRAS, 476, 943
Igo, Z., Parker, M. L., Matzeu, G. A., et al. 2020, MNRAS, 493, 1088
Kaastra, J. S., Kriss, G. A., Cappi, M., et al. 2014, Sci, 345, 64
Kaastra, J. S., Mewe, R., Liedahl, D. A., Komossa, S., & Brinkman, A. C. 2000, A&A, 354, L83
Kalberla, P. M. W., Burton, W. B., Hartmann, D., et al. 2005, A&A, 440, 775
Kallman, T., Liedahl, D., Osterheld, A., Goldstein, W., & Kahn, S. 1996, ApJ, 465, 994
Kaspi, S., et al. 2002, ApJ, 574, 643
Kaspi, S., Netzer, H., Chelouche, D., et al. 2004, ApJ, 611, 68
King, A. R. 2003, ApJL, 596, L27
King, A. R. 2010, MNRAS, 402, 1516
Kosec, P., Buisson, D. J. K., Parker, M. L., et al. 2018, MNRAS, 481, 947
Kriss, G. A., de Rosa, G., Ely, J., et al. 2019, ApJ, 881, 153
Kriss, G. A., Lee, J. C., Danehkar, A., et al. 2018, ApJ, 853, 166
Longinotti, A. L., Kriss, G., Krongold, Y., et al. 2019, ApJ, 875, 150
Longinotti, A. L., Krongold, Y., Guainazzi, M., et al. 2015, ApJ, 813, 39
Maiolino, R., Risaliti, G., Salvati, M., et al. 2010, A&A, 517, A47
Matzeu, G. A., Reeves, J. N., Braito, V., et al. 2017a, MNRAS, 472, L15
Matzeu, G. A., Reeves, J. N., Nardini, E., et al. 2016, MNRAS, 458, 1311
Matzeu, G. A., Reeves, J. N., Nardini, E., et al. 2017b, MNRAS, 465, 2804
McKernan, B., Yaqoob, T., & Reynolds, C. S. 2007, MNRAS, 379, 1359
Mehdipour, M., Kaastra, J. S., Kriss, G. A., et al. 2017, A&A, 607, A28
Nardini, E., Reeves, J. N., Gofford, J., et al. 2015, Sci, 347, 860
Parker, M. L., Longinotti, A. L., Schartel, N., et al. 2019, MNRAS, 490, 683
Parker, M. L., Pinto, C., Fabian, A. C., et al. 2017, Natur, 543, 83
Parker, M. L., Reeves, J. N., Matzeu, G. A., Buisson, D. J. K., & Fabian, A. C. 2018, MNRAS, 474, 108
Pinto, C., Alston, W., Parker, M. L., et al. 2018, MNRAS, 476, 1021
Pounds, K., Lobban, A., Reeves, J., et al. 2016, MNRAS, 457, 2951
Pounds, K. A., & King, A. R. 2013, MNRAS, 433, 1369
Pounds, K. A., Reeves, J. N., King, A. R., et al. 2003, MNRAS, 345, 705
Pounds, K. A., & Vaughan, S. 2011, MNRAS, 413, 1251
Reeves, J. N., & Braito, V. 2019, ApJ, 884, 80
Reeves, J. N., Braito, V., Gofford, J., et al. 2014, ApJ, 780, 45
Reeves, J. N., Braito, V., Nardini, E., et al. 2016, ApJ, 824, 20
Reeves, J. N., Braito, V., Nardini, E., et al. 2018a, ApJL, 854, L8
Reeves, J. N., Braito, V., Nardini, E., et al. 2018b, ApJ, 867, 38
Reeves, J. N., Lobban, A., & Pounds, K. A. 2018, ApJ, 854, 28
Reeves, J. N., O'Brien, P. T., Braito, V., et al. 2009, ApJ, 701, 493
Reeves, J. N., O'Brien, P. T., & Ward, M. J. 2003, ApJL, 593, L65
Reeves, J. N., Wynn, G., O'Brien, P. T., et al. 2002, MNRAS, 336, L56
Saez, C., & Chartas, G. 2011, ApJ, 737, 91
Sanfrutos, M., Longinotti, A. L., Krongold, Y., et al. 2018, ApJ, 868, 111
Serafinelli, R., Tombesi, F., Vagnetti, F., et al. 2019, A&A, 627, A121
Sirressi, M., Cicone, C., Severgnini, P., et al. 2019, MNRAS, 489, 1927
Tombesi, F., Cappi, M., Reeves, J. N., et al. 2010, A&A, 521, A57
Tombesi, F., Cappi, M., Reeves, J. N., et al. 2011, ApJ, 742, 44
Tombesi, F., Cappi, M., Reeves, J. N., et al. 2012, MNRAS, 422, L1
Torres, C. A. O., Quast, G. R., Coziol, R., et al. 1997, ApJL, 488, L19
Turner, T. J., Reeves, J. N., Braito, V., et al. 2018, MNRAS, 481, 2470
Wilms, J., Allen, A., & McCray, R. 2000, ApJ, 542, 914